NANO LETTERS

2009
Vol. 9, No. 9
3116-3123

Parametric Nanomechanical Amplification at Very High Frequency

R. B. Karabalin, X. L. Feng, and M. L. Roukes*

Kavli Nanoscience Institute, California Institute of Technology, Mail Code 114-36, Pasadena, California 91125

Received April 3, 2009; Revised Manuscript Received June 19, 2009

ABSTRACT

Parametric resonance and amplification are important in both fundamental physics and technological applications. Here we report very high frequency (VHF) parametric resonators and mechanical-domain amplifiers based on nanoelectromechanical systems (NEMS). Compound mechanical nanostructures patterned by multilayer, top-down nanofabrication are read out by a novel scheme that parametrically modulates longitudinal stress in doubly clamped beam NEMS resonators. Parametric pumping and signal amplification are demonstrated for VHF resonators up to ~130 MHz and provide useful enhancement of both resonance signal amplitude and quality factor. We find that Joule heating and reduced thermal conductance in these nanostructures ultimately impose an upper limit to device performance. We develop a theoretical model to account for both the parametric response and nonequilibrium thermal transport in these composite nanostructures. The results closely conform to our experimental observations, elucidate the frequency and threshold-voltage scaling in parametric VHF NEMS resonators and sensors, and establish the ultimate sensitivity limits of this approach.

Parametric resonance, unlike an ordinary driven resonance, is excited by time-varying modification of a system parameter.[1] A classic example is a swinging gymnast who stands and squats twice during each period of oscillation, thereby modulating the oscillator's effective length, to sustain the oscillatory motion. Parametric resonant systems have been an interesting research subject in many areas that range from quantum optics,[2] to plasma[3] and superconducting physics,[4] to electronics and radio-wave engineering.[5] In the domain of miniaturized mechanical structures, a parametric amplifier was first demonstrated using a ~34kHz microcantilever for thermomechanical noise squeezing.[6] Thereafter considerable attention has been drawn to studying parametric resonances in micromachined electromechanical systems (MEMS).[7−11] The simplest parametric amplification in mechanical resonators is obtained by periodically modulating the spring constant (i.e., stiffness) at twice its fundamental resonance frequency. An increase in amplitude and effective quality factor can be achieved if appropriate phase relation is coordinated between the driving and parametric pumping signals. Modulation of spring constants of MEMS resonators have often been realized capacitively,[7−9] although other schemes such as exploiting intrinsic residual stress[10] or employing an external feedback loop[12] have also been demonstrated.

At the nanometer scale, resonant nanoelectromechanical systems (NEMS)[13] offer new advantages such as ultrahigh frequencies,[13,14] ultrahigh responsivities and sensitivities,[13,15,16] and the operation at ultralow power levels.[16,17] These make NEMS resonators, especially those operating at high frequencies, promising for resonant sensing[15−17] and precision measurement.[18] However, NEMS signal transduction is often limited by the noise floor of the preamplifiers employed as electronic readouts, and this is often true even with use of cryogenic amplifiers with very low noise figures.[17,19] The intrinsic fluctuations of high frequency NEMS transducers are at such a low level that noise mismatch at the first readout stage compromises their sensitivity and useable dynamic range (DR)[20] and, thus, often imposes significant practical limitations on their performance.[17,19] A fundamental solution to this challenge is direct amplification of a device's signal in the mechanical domain by parametric phenomena, before electronic amplification is employed. In this work, we explore such mechanical-domain signal amplification with very high frequency (VHF) (>30 MHz) NEMS resonators for the first time. Further, we investigate the frequency scalability and parasitic effects imposed by practical materials and by device design and geometry.

Figure 1a shows a typical VHF resonant NEMS parametric amplifier used in our experiments. The design is based on mechanically coupled beams: the "H"-shaped structure consists of a signal beam (center) supported by two pump beams. As illustrated in Figure 1b, by applying periodical force to the pump beams, we can effectively vary the signal beam's tension and thus modulate its spring constant. This design was first proposed by Harrington and Roukes and was initially demonstrated in a larger resonator operating at HF

* Corresponding author. E-mail: roukes@caltech.edu.

10.1021/nl901057c CCC: $40.75
Published on Web 08/04/2009

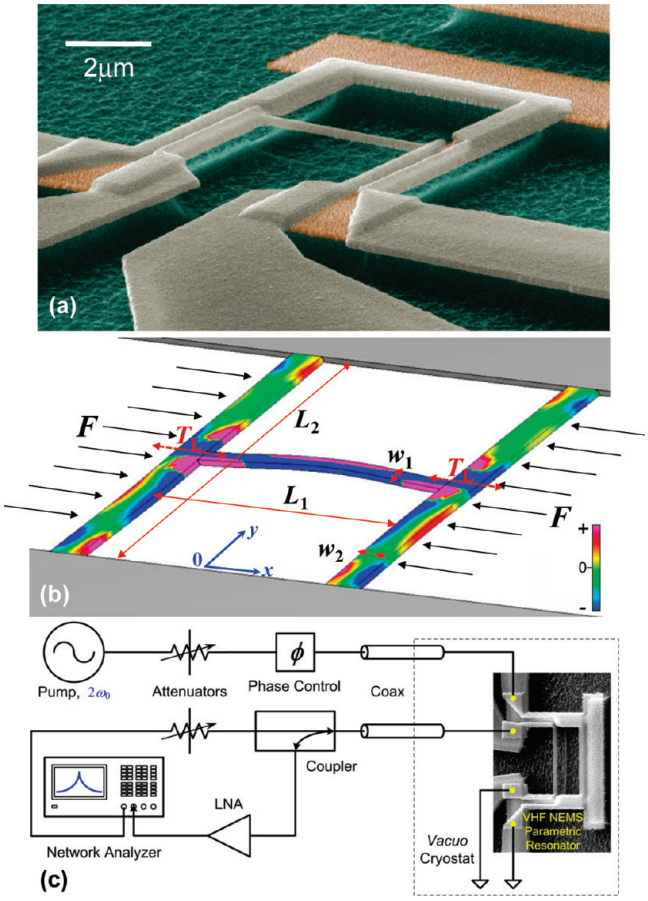

Figure 1. Very high frequency (VHF) nanomechanical parametric resonators based on H-shaped complex structures. (a) Scanning electron microscopy (SEM) image (colorized) showing a suspended device fabricated in a multilayer lithographical surface nanomachining process. (b) Illustration of the principle of device design based on mechanically coupled beams, demonstrating how the longitudinal tension (T_L) in the signal beam can be tuned by the in-plane forces applied to the pump (support) beams. The finite element simulation results show the strain distribution (color mapped) in the deflected structure. (c) Schematic showing the experimental setup and simplified circuitry for VHF measurements.

(high frequency, ~17 MHz).[21] To realize VHF devices, we have developed a new two-step lithographic and surface nanomachining process. This has enabled scaling the device downward by a factor of ~5 in linear dimension, which corresponds to a ~100-fold reduction in volume and mass. Starting from 80 nm SiC epilayer heteroepitaxially grown on Si, we first pattern the structural layer for the pump beams via electron-beam lithography (EBL), followed by electron-beam evaporation of 70 nm SiO_2 and liftoff. Next, the signal beam and the pump beams' electrical paths are patterned in a second EBL step, then metallized by 5 nm Ti on top of 40 nm Al, and subsequently processed by conventional liftoff. The device is then suspended by a dry etch process in a microwave-coupled plasma using Ar and NF_3, first anisotropically (by vertically etching through the SiC layer) and then isotropically (by subsequently etching the sacrificial Si layer). As shown in Figure 1a, the SiO_2 layer (orange) serves to electrically isolate the conducting paths (gray) atop the signal and pump beams. The major advantage of this process is that the device is suspended in a single final dry etch; hence, no wet processing or subsequent patterning is required after device release. We note that based on chemically synthesized bottom-up nanowire structures, parametrically excited resonators[22] and high-performance VHF resonators[23] have recently also been realized. However our top-down surface nanomachining approach is unique in enabling multilayer devices with much greater structural and geometrical complexity and, hence, functionality and control, especially for parametric systems.

The design shown in Figure 1 is well suited for in-plane actuation of the beams via the Lorentz force induced magnetomotively. Magnetomotive actuation and detection[14,16,17,19] have proven to be highly efficient for VHF and ultrahigh frequency (UHF) NEMS.[17] Figure 1b illustrates the typical geometry: AC current flowing in thin-film electrodes induce, when in the presence of an out-of-plane magnetic field, an in-plane Lorentz force and thereby in-plane beam deflection. Typical results of a finite-element simulation for these forces are presented in a color map.[24] In our experiments, the devices are placed in a vacuum cryostat cooled in liquid helium, and immersed in a strong magnetic field B (up to 8 T) for magnetomotive transduction. When alternating current $I(t)$ is passed through the beam electrode of length L in magnetic field Lorentz force $F = LBI(t)$ is generated, thereby exciting the vibration of beam. The motion of the NEMS beam in the B field generates electromotive-force (EMF) voltage $V_{EMF}(t) = \xi LB\mathrm{d}y(t)/\mathrm{d}t$ across the vibrating beam's electrode (here $y(t)$ is the displacement and ξ is a geometrical factor that depends on the mode shape).[25] The magnetomotively transduced device motion is modeled as a parallel RLC circuit;[25] device vibration near resonance strongly changes the electrical impedance. This allows us to detect the device's electromechanical response by using radio frequency (RF) reflectometry measurements, a well established technique in RF/microwave engineering and has also been widely employed in high-frequency electronic readout of various nanodevices.[16,18,25,26] Figure 1c depicts the schematic of experimental setup and readout circuitry. The parametric pump is induced by RF current at twice the resonance frequency sent through the pumping beams. The Lorentz force in the pumping beams exerts longitudinal force upon the signal beam.

Parametric modulation of the longitudinal tensile stress in a doubly clamped beam results in periodic modulation of its fundamental-mode resonance frequency[27] according to the equation

$$f_0 \equiv \frac{\omega_0}{2\pi} = \left(1.03\frac{w}{L^2}\sqrt{\frac{E_Y}{\rho}}\right)\sqrt{1 + \frac{\sigma L^2}{3.4E_Y w^2}} \qquad (1)$$

where L is the beam length, E_Y is the elastic (Young's) modulus, ρ is the density, w is the dimension in the direction of vibration (width in this case), and σ is the tensile stress. Modeling the behavior of the beam's central point as a single degree-of-freedom harmonic oscillator with effective mass m, intrinsic linear spring constant k_1, quality factor Q, and

with Duffing nonlinearity characterized by cubic term, k_3,[1] we obtain the following equation of motion

$$m\ddot{x} + \frac{m\omega_0}{Q}\dot{x} + (k_1 + k_p\cos(2\omega_0 t))x + k_3 x^3 = F_0\cos(\omega_0 t + \varphi) \tag{2}$$

Here $k_p \cos(2\omega_0 t)$ is the periodic modulation of the linear spring constant by parametric pumping. The parametric modulation is imposed at twice the device's resonance frequency, hence the amplitude of the motion is amplified and the gain is given by

$$G = \frac{A_{\text{pumpon}}}{A_{\text{pumpoff}}} = \left[\frac{\cos^2(\phi + \pi/4)}{(1 + k_p/k_t)^2} + \frac{\sin^2(\phi + \pi/4)}{(1 - k_p/k_t)^2}\right]^{1/2} \tag{3}$$

where $k_t = 2k_1/Q$ is the threshold parametric pump. While the second term diverges as k_p approaches k_t, the intrinsic nonlinearities set a limit to the amplitude increase.[10] In addition to the amplitude increase, parametric amplification also results in Q enhancement. As the pump is increased the resonance peak becomes substantially higher and narrower and assumes a non-Lorentzian form[28]

$$A = \frac{F_0 Q}{m\omega_0^2}\cdot\frac{2Q(\omega_D - \omega_0) - i\omega_0}{\dfrac{-4Q^2}{\omega_0(\omega_D - \omega_0)^2} + 4iQ(\omega_D - \omega_0) + \omega_0\left(1 - \dfrac{k_p^2}{k_t^2}\right)} \tag{4}$$

As displayed in Figure 1 in the H-shaped structure of the device, the signal beam has dimensions of length L_1, width w_1, and thickness t_1; likewise, the two pump beams have dimensions L_2, w_2, and t_2. When an electrical current passes through the pump beams' electrodes the magnetomotive effect induces in-plane Lorentz forces, which alter the signal beam's longitudinal tensile stress. Application of a DC current will induce a shift in the resonance frequency. The corresponding spring constant change is

$$k_p = \frac{0.3k_1 L_1^2\sigma}{E_Y w_1^2} \tag{5}$$

For a DC current I_{DC} passing through the pump beams in magnetic field B, the longitudinal tensile force is

$$T_L = \sigma w_1 t_1 = -2BI_{DC}L_2\gamma = -\frac{2BL_2\gamma}{R_{\text{pump}}}V_{DC} \tag{6}$$

where $\gamma = 0.23$ is a geometrical factor that accounts for the finite stiffness of the pump beams. R_{pump} is the ohmic resistance of the pump beams' electrode (typically 50−100 Ω) and V_{DC} is the voltage drop across it. We perform finite element simulations[24] to determine γ and to optimize the resonator's geometry (see Figure 1b). As a result, the fractional frequency shift due to this force is

$$\frac{\delta f}{f} = \frac{k_p}{2k_1} = -\frac{0.3BL_1^2L_2\gamma}{E_Y w_1^3 t_1 R_{\text{pump}}}V = -\eta V \tag{7}$$

where the coefficient η depends only on magnetic field, and the choice of material and geometry for the device. The subscript "DC" in voltage (V) is intentionally removed because the equation is valid for both DC and RF voltages. Since threshold stiffness modulation is $k_t = 2k_1/Q$, the threshold voltage is

$$V_t = \frac{1}{\eta Q} \tag{8}$$

We first characterize the tunability of the signal beam's resonance frequency via the Lorentz force by applying a DC current through the pump beams. The sample assembly is kept at an ambient temperature of ∼10 K. As illustrated in Figure 2a, DC bias voltages with positive and negative polarities are applied across the pump beams to induce both tensile and compressive tension in the signal beam. Figure 2b shows that regardless of the bias polarization the measured resonant frequency of the signal beam is tuned downward. This downward frequency tuning is asymmetric with respect to the applied bias voltage. Careful, repeated measurements indicate that this is a superposition of two components: linear frequency tuning due to the Lorentz force (eq 7), and a symmetric downward tuning with increasing DC current due to Joule heating of the device. Our metallized SiC NEMS resonators have negative frequency−temperature coefficients in this temperature range,[29] and Joule heating is solely dependent upon the magnitude of the applied DC bias and is independent of the sign (direction) of the current flow. Examination of the change in Q with increasing DC bias, as shown in Figure 2c, confirms that the symmetric downward tuning arises from heating. Using experimental parameters for this device, this heating effect can be quantitatively modeled and subtracted, allowing extraction of the linear frequency tuning due to induced longitudinal tension in the signal beam via the Lorentz force (eq 7). The result is shown in Figure 2d; the blue straight line is a theoretical prediction using the known geometrical parameters of this VHF NEMS device.

Parametric amplification is induced by biasing the pump beams with an RF signal. The expected response is calculable given our calibration of pumping, tuning, and heating in the DC tests described above. We first calibrate the resonance frequency shift and Q change of the signal beam due to Joule heating by the RF pump (with increasing power, but off the twice resonance frequency $2f_0$ by several times of f_0/Q). We then bias the pump beams at twice the calibrated resonance frequency, and perform careful reflectometry measurements of the signal beam's resonance. Figure 3 demonstrates the experimental data. Both resonance signal increase (amplification) and peak narrowing (Q-enhancement) are clearly observed. The shapes of the curves closely match the theoretical prediction of eq 4. The Q enhancement we observe is partially compromised by the fact that Q

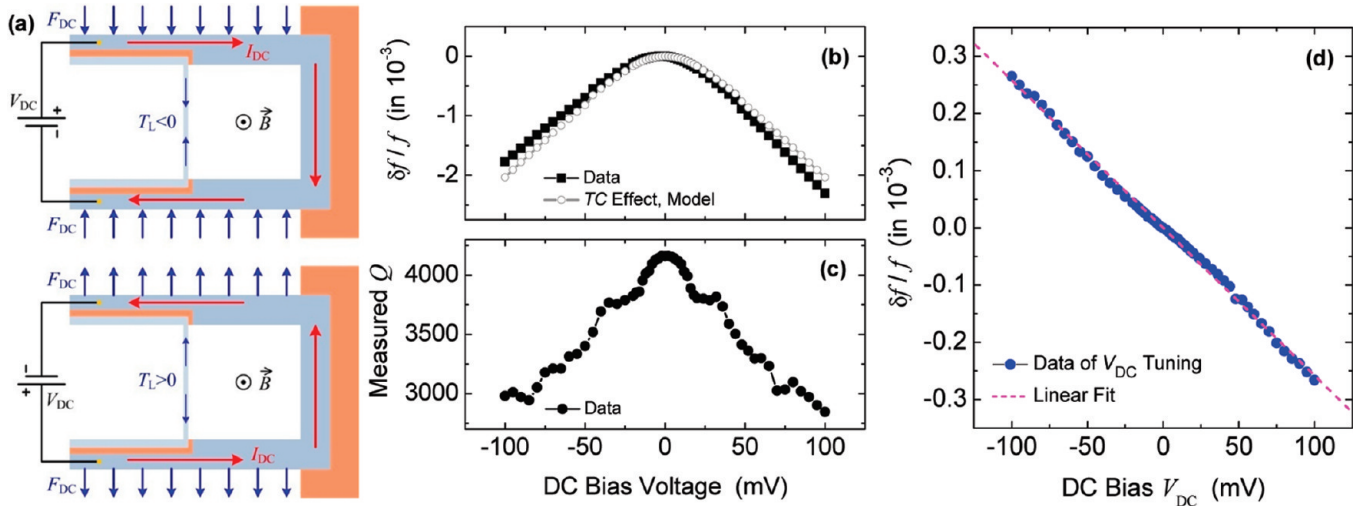

Figure 2. Frequency tuning and heating effects with pump beams under DC bias. (a) Schematic illustrating the DC bias of pump beams with different polarizations, forces induced in the pump beams and the resultant tension in the signal beam. (b) Measured fractional resonance frequency shift as a function of DC bias. Data trace with hollow circles is calculated fractional frequency shift due to Joule heating effect caused by DC bias, by employing experimentally measured temperature coefficient (TC) of resonance frequency from such devices. (c) Measured quality factor (Q) of the signal beam as a function of DC bias. The decrease in Q and the symmetric tendency of the curve verifies the DC bias induced heating effect and the symmetric frequency down shift caused by heating. (d) Linear frequency tuning by the Lorentz forces applied on the pump beams at DC bias.

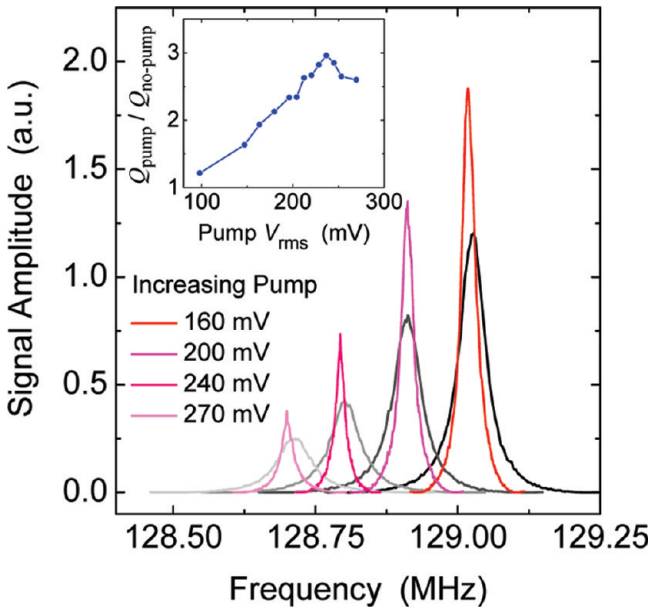

Figure 3. Experimental data of resonance signal amplification and Q enhancement under parametric pumping for a ~130 MHz resonance. The main plot shows the response under parametric pumping has increased amplitude and narrower peak. The parasitic frequency shift with increasing parametric pumping is due to the heating-up of the signal beam when the supporting beams are parametrically pumped at high levels. The inset shows the increase of measured Q as a function of the rms pumping voltage.

decreases with RF heating as the pump voltage is increased. Hence, the threshold pumping voltage increases, according to eq 8. Without any RF bias power on the pump beams, the initial Q of the signal beam is measured to be ~4000; but when enough bias power (at frequency off $2f_0$) is applied, the initial, unpumped Q drops to ~2500 at $V_{rms} = 100$ mV and further drops to ~1700 at $V_{rms} = 280$ mV. The maximum Q enhancement is thus observed at pump voltage of $V_{rms} =$ 240 mV; in this case Q increases from ~2300 to ~6900 with pumping frequency from off $2f_0$ to at $2f_0$, respectively. These DC tuning and RF parametric pumping experiments both strongly suggest that "parasitic" f_0 and Q alterations arising from Joule heating are concomitant with the desired Lorentz-force-induced tuning and pumping effects.

We believe this trade-off between the induction of parametric phenomena and the deleterious Joule heating at large pump power is generic. It is interesting, however, that this effect was not reported in a preliminary study focused upon similar devices with much larger size.[21] We believe that this contrast reflects fundamental aspects of dimensional scaling for Lorentz-force mechanical parametric amplifiers. Nonetheless, we note that, even the seemingly quite modest enhancement by the present parametric amplifier can be very useful. Particularly for resonant mass sensors, a NEMS parametric amplifier with gain of only 3 improves the attainable dynamic range by ~10 dB and thus the mass sensitivity[30] by a factor of 3. This may immediately lead to a dramatic difference at the levels where NEMS sensors already offer few- to single-molecule sensitivities[16,17] to further enable the capability of distinguishing one single molecule from another.

To maintain performance while scaling operating frequency upward (through a downscaling of size), it is essential to understand heating and thermal transport in these compound nanostructures. To determine the practical limits of Lorentz-force parametric amplifiers, we have developed a thermal transport model allowing calculations of the heat transfer rates between all the important nodes of heat flows in these compound NEMS devices. Figure 4 illustrates the components of our model. We assume, with application of electrical bias, uniform Joule heating occurs within the metallic electrodes atop the pump beams. We further assume

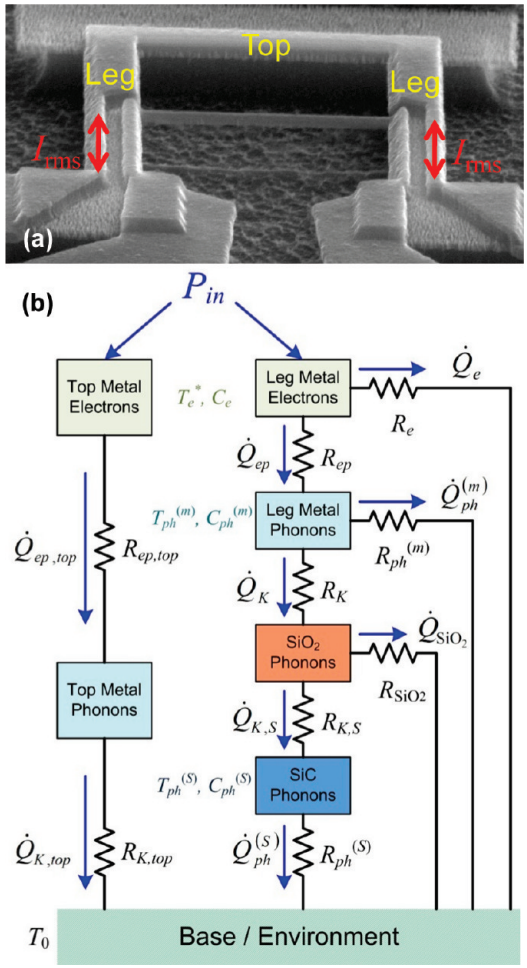

Figure 4. Joule heating and thermal transport in the H-shaped VHF NEMS parametric resonator. (a) Illustration of the structure, in which noticeable joule heating (via I_{rms}) occurs first in the pumping beams (consisting of the segments labeled "top" and "leg") at high pumping power levels. (b) The thermal model illustrating the thermal conduction pathways through which the joule heating power is dissipated to the device substrate which is at the base temperature.

that a steady-state electron temperature is established within these metal electrodes. Electron−phonon scattering from these hot electrons then heats the phonons in the metal lattice, and we characterize this internal thermal transfer with an electron−phonon conductance G_{ep}.[31] The metal lattice phonons subsequently transfer heat to the dielectric SiO_2 layer beneath through the Kapitza thermal boundary conductance G_K and, subsequently, to the SiC structural layer through its much larger conductance G_{KS} which we neglect.[32,33] Finally the incoming power and lateral dissipation rate into the clamping points and substrate (assumed to be at base temperature T_0) determine the temperature profile of each pump beam. Additionally, each intermediate thermal pathway is associated with a parallel (lateral) pathway directly to the substrate. All of these thermal pathways must be taken into account in the calculation. We have found the top metal electrode (labeled "top" in Figure 4a) on the pump beams attains a negligibly small temperature difference from the substrate temperature due to the large values of G_K and G_{KS}.

The electron thermal conductivity for heat flow from the metal electrodes directly into the substrate (T_0) is estimated from Wiedemann−Franz law via the Sommerfeld model[34]

$$\kappa_e = \frac{\pi^2}{3}\left(\frac{k_B}{e}\right)^2 \sigma_e T \tag{9}$$

Here k_B and e are the Boltzmann constant and electron charge, respectively. The thermal conductance associated with metal electrons is then

$$G_e = \frac{\pi^2}{3}\left(\frac{k_B}{e}\right)^2 \sigma_e \frac{A_{pump}}{L_{pump}} T \tag{10}$$

Here the electrical conductivity $\sigma_e = L_{pump}/(A_{pump}R_{pump})$ is estimated for each specific geometry and operating condition; A_{pump} and L_{pump} are the cross-sectional area and length of the pump electrode, respectively. In practice, σ_e is evaluated by integration over the nonuniform geometry (width) of the pumping beams (see Figure 1 or 4a). The heat flux is then calculated as

$$\dot{Q}_e = \int_{T_0}^{T_e} G_e \, dT \tag{11}$$

The thermal conductance associated with heat transfer between electrons and phonons in the metal is

$$G_{ep} = c_e(T)\Gamma_{ep}(T)V_{eff} \tag{12}$$

where $c_e(T) = (\pi^2/2)(nk_B^2/\varepsilon_F)T$ is the electron heat capacity per unit volume, calculated using the Sommerfeld model;[34] and n and ε_F are the number density and Fermi energy of the metal electrons, respectively. Here V_{eff} is the effective volume and Γ_{ep} is the relevant electron−phonon scattering rate, given by[31]

$$\Gamma_{ep} = \frac{4\zeta(3)}{3\pi}\frac{k_B^3\varepsilon_F^2}{\hbar^4 v_s^4 v_F \rho}T^3 \tag{13}$$

Here v_s is the velocity of sound and $\zeta(x)$ is a Riemann function with $\zeta(3) = 1.202$; v_F is the Fermi velocity and $\hbar$ is the Planck constant.

Special care must be taken when evaluating the heat flux that escapes the resonator through the ends of the pump beams. This calculation is valid for both the Al metallization and the SiC structural layers, if appropriate parameters are utilized for each. We assume the power generation is uniformly distributed in the metal layer, and then solve the thermal transfer differential equation

$$\kappa\frac{d^2T}{dy^2} = \frac{\dot{Q}_{lat}}{L_2 w_{2eff} t_{metal}} \tag{14}$$

Here subscripts for thermal conductivity κ and lateral heat flux $\dot{Q}_{lat}$ are intentionally omitted as the equation separately

applies to both the Al and SiC layers. We impose the boundary conditions $T = T_0$ at $y = 0$ and $y = L_2$ (see system coordinates in Figure 1b), as noted earlier. On the basis of previous studies of thermal transport in nanoscale beams,[35] the thermal conductivity is estimated assuming a simple diffusive model $\kappa \approx c_v v_s \Lambda/3 = \alpha_p T^3$. Here c_v is the heat capacity per unit volume, calculated using Debye model $c_v = (12/5)\pi^4 k_B n (T/T_D)^3$ with n being the number density of atoms. In light of these previous studies, we assume the effective phonon mean free path is limited by boundary scattering and can be approximated by the relation $\Lambda \approx 1.12\sqrt{A}$, where A is the smallest cross section of the beam. The formulas we deduce here are valid for temperatures below 40−50 K, which is suitable for our case ($T_0 \approx 10$ K). If temperature rises beyond this range, the expected heating will be stronger than the model predicts, because at elevated temperatures the thermal conductances saturate. In this case, the estimated temperature would be lower than what is experienced in experiment.

From the thermal diffusion eq 14, we obtain the steady-state spatial temperature profile

$$T(y) = \sqrt{T_0^2 - 2\beta\frac{y^2}{L_2^2} + 2\beta\frac{y}{L_2}} \tag{15}$$

where $\beta = (T_0^4 + \dot{Q}_{lat} L_2/\alpha_p w_{2eff} t_{metal})^{1/2}$. Equation 15 indicates that uniformly distributed Joule heating in Al wire, whose ends are held at constant temperature, yields a parabolic-shaped temperature distribution for the electrons in the metal. Hot metal electrons subsequently heat metal phonons according to eqs 12 and 13. To calculate the associated heat flux, we assume uniform power distribution, where electrons are at numerically calculated average temperatures based on distribution given by eq 15. A similar procedure is performed for subsequent lateral thermal pathways in Figure 4. The culmination of this process is that phonons within the SiC layer attain a similar, elevated temperature profile with a maximum at the center of each pump beam. As a result, the signal beam becomes uniformly thermalized to precisely the peak temperature of the pump beam (given by eq 15). The expression for SiC layer phonon thermal conductance is then

$$G_{ph} = 8\frac{\alpha_p w_2 t_2}{L_2} T(2T^2 - T_0^2) \tag{16}$$

We now turn to consider heat conductance between phonons in the metallic and structural layers. The thermal transport between two solid materials at low temperatures has been studied in past decades both experimentally and theoretically. Two theoretical models, the acoustic mismatch model and diffusive mismatch model,[32] adequately explain solid−solid thermal boundary resistance. The Kapitza conductance is given by

$$G_K = 4\sigma_K A_{metal} T^3 \tag{17}$$

where $\sigma_K = 900\text{W/m}^2\text{ K}^4$ (for SiO_2−Al boundary[32]) is a constant parameter that depends only on the nature of the contacting materials; A_{metal} is the overlapping contact area of the metal electrode. For temperatures above 10 K, this value is at least 10 times larger than $G_{ph}^{(R)}$ of structural layer phonon thermal conductance. Previous studies of Kapitza conductance coefficient for SiO_2−Si boundary[33] yield a value $\sigma_K = 9000\text{W/m}^2\text{ K}^4$, which is an order of magnitude higher. Therefore we treat SiO_2 and SiC as a single layer. These considerations yield five equations with the form of eq 11 for the thermal paths in Figure 4. Their corresponding relations are

$$\begin{aligned} \dot{Q}_{ep} &= \dot{Q}_{ph}^{(m)} + \dot{Q}_K \\ \dot{Q}_K &= \dot{Q}_{ph}^{(s)} \\ P_{leg} &= \dot{Q}_e + \dot{Q}_{ep} \end{aligned} \tag{18}$$

Here superscripts "m" and "s" indicate metal and structural layers, respectively; subscripts "ep" and "ph" indicates electron−phonon and phonon, respectively. Solving these equations numerically yields the temperature of the NEMS resonator (signal beam) which depends on applied pump power that is dissipated in the pump beams. We can now use this to evaluate the trade-off between the enhanced parametric actuation and the undesirable increase of parametric threshold voltage V_t, as pump power is increased. In order to validate the model, experiments were performed in which the resonance frequency dependence on sample temperature was measured. When pumping power is applied to the pump beams, the signal beam's resonance frequency serves as an embedded thermometer. The green triangles in Figure 5a are the observed frequency shift when the sample is temperature-regulated and its temperature measured by a precise sensor mounted in close proximity of the device. Also shown is the resonance frequency shift versus temperature rise due to applied DC and RF pumping, which is evaluated using the above thermal model. The good agreement confirms that the model reliably predicts the temperature of the device.

We now analyze and evaluate the scalability of such VHF NEMS parametric amplifiers. Equation 8 indicates that the threshold voltage of parametric amplification is inversely proportional to Q. On the basis of previous experimental studies of temperature dependent dissipation in NEMS resonators,[29,36] we assume Q scales as $T^{-0.3}$ for SiC NEMS. Combining this with our Joule heating model, we build a link from a given applied pumping voltage to the Q degradation. Figure 5b shows the predicted Q in comparison with what we measure experimentally when the device is heated via DC and RF pumping voltages or by directly heating the sample. The dashed line shown here is the $Q \sim T^{-0.3}$ empirical relation. The model correctly predicts Q values up to 40−50 K (at pumping voltage ~200 mV); beyond this point dissipation grows even faster at higher temperatures.

Taking into account the thermal transport model and the empirical Q dependency on temperature, we estimate the threshold voltage V_t for parametric amplification at given Joule heating power input. The experimental threshold voltage is determined by fitting measured Q-enhanced curves

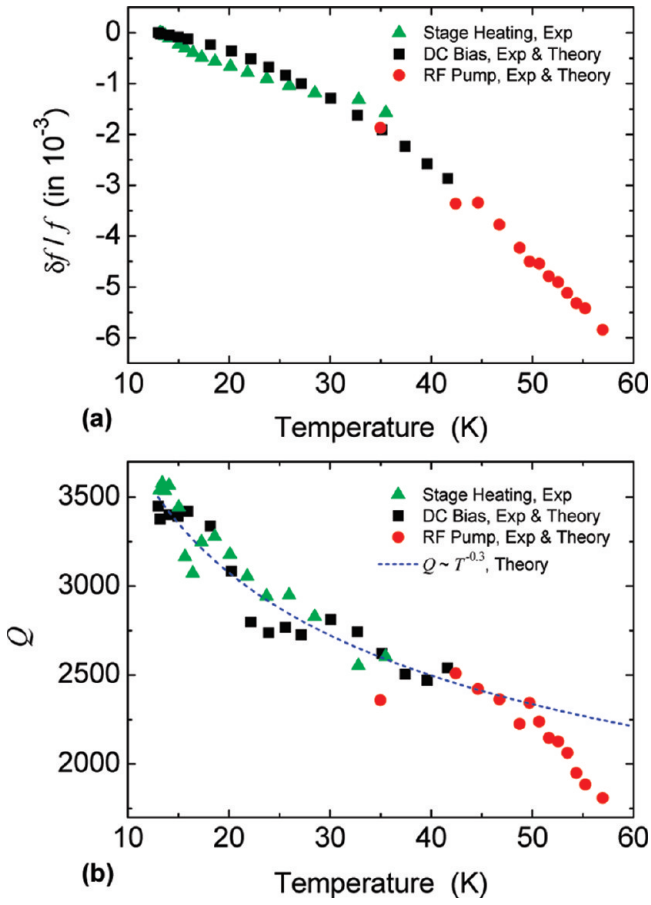

Figure 5. Validation of the thermal model with the measured frequency shift and Q change. (a) Fractional frequency shift and (b) Q. Three methods of device heating were used: (1) the device temperature was increased via the temperature-regulated device stage (green triangles), (2) the device was heated via a DC bias through the pump beams (black squares), and (3) the device was heated via RF pumping (red circles). For the latter two cases, the device temperature was determined via the thermal model presented here. The measured Q (b) also suggests that above 50 K the actual temperature may rise faster than the thermal mode predicts, as the measured Q appears to be reduced faster than the empirically predicted $Q \sim T^{-0.3}$ law.

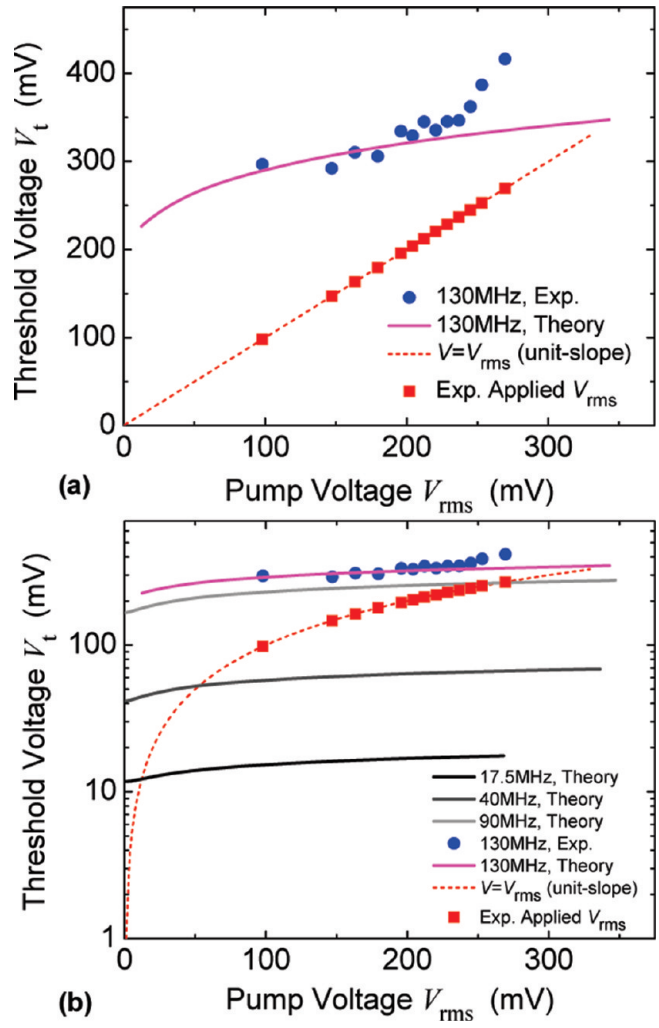

Figure 6. Scaling of the parametric pumping threshold voltage and the heating effect in the composite nanostructure. (a) Linear-scale plot showing threshold voltage dependence on applied pumping voltage for the 130 MHz device, with both experimental data and the calculation with the thermal model taking into account the device temperature rise due to joule heating and reduced thermal conductance. The applied RF pump voltage is a unit−slope (45°) line on this plot. (b) Semilogarithmic-scale plot showing the scaling of threshold voltage for 17.5, 40, 90, and 130 MHz devices with various dimensions.

to theoretical predictions given by eq 4. Figure 6a shows the scaling of the threshold voltage as a function of the applied pumping voltage with both experimental and theoretical data for the 130 MHz device. The applied voltage is also represented by the straight line (red) of unit-slope (45°). The intersection point between the threshold voltage curve and the 45° line signifies the accessible threshold voltage. The plot in Figure 6a explains the Q enhancement that we have observed quite well. Initially, approaching the threshold, the closest case is $k_p/k_t \approx 0.7$ for $V_{rms} = 240$ mV where Q increases from ~2300 to ~6900. At higher pumping voltages the threshold increases faster because of a faster drop in Q. The experimental data agree well with the predictions of our model for temperatures below 40−50 K. In order to attain large amplification gain for this device, the signal beam would be heated up by at least 50 K, causing the parametric threshold to become hardly accessible.

The result in Figure 6a manifests that achieving the threshold voltage for the 130 MHz device is accompanied by noticeable heating of the beam because of the reduced thermal conduction in the composite nanostructure. We extend our threshold voltage modeling to several other geometries of the similar H-shaped coupled-beams design and of the same multilayer material stacking. These include a 17.5 MHz device with dimensions of $L_1 = 10.5$ μm, $w_1 =$ 300 nm, $L_2 = 17.5$ μm, $w_2 = 1$ μm, a 40 MHz device with $L_1 = 5.5$ μm, $w_1 = 200$ nm, $L_2 = 7.5$ μm, $w_2 = 700$ nm, and a 90 MHz device with $L_1 = 4$ μm, $w_1 = 200$ nm, $L_2 =$ 6.5 μm, $w_2 = 700$ nm. Figure 6b demonstrates the scaling of the threshold voltage of all these devices in a semilogarithm scale along with experimental data from the 130 MHz device. For all these devices, the threshold scales up with increasing pumping voltage. Clearly this imposes practical limits on the devices' performance in achieving the ideal parametric amplification above threshold. We note that these limitations occur primarily at low temperatures where the

thermal conductance in the nanobeam or nanowire structures is generally strongly reduced compared to bulk values.[35,37] However we expect that the temperature rise and Q drop at elevated temperatures would be considerably diminished given the much smaller reduction in device thermal conductance.

In summary, we have demonstrated ~130 MHz VHF NEMS parametric resonator and amplifier. We have identified and investigated the interesting Joule heating due to the reduced thermal conductance in composite nanodevices. As we shrink the devices, Q and parametric threshold voltage V_t are no longer constants, but scale down (Q) and up (V_t) respectively with increasing parametric pumping voltage. Eventually, the competing effects due both to parametric pumping and to heating together determine the device performance.

Our experiments and analysis clarify several issues important for attaining ideal parametric amplification and operations above threshold with very small VHF NEMS devices. First, it would be desirable to engineer materials that provide and preserve high thermal conductivities when scaling from bulk to nanostructures. Second, it is preferred to employ materials that have very low internal friction and temperature-insensitive dissipation (i.e., $Q \sim T^{-\alpha}$ with α approaching zero). Third, it would also be desirable to engineer devices with negligible frequency−temperature coefficient in the temperature range of interest, in order to minimize the resonance frequency shift with increasing parametric pump.

The most important applications of NEMS parametric amplifiers are perhaps noise matching in high-precision measurement[17−19] and in sensing,[8,15−17,30,38] where some of the most promising devices are flexural-mode nanobeams and nanowires vibrating in the frequency range of ~100 MHz−1 GHz.[14,16,17,23] Realizing NEMS parametric amplifiers with ideal mechanical gain and thermomechanical noise matching at >100 MHz remains a challenging prospect. We anticipate that advances can be made by employing both new materials (e.g., thin-film diamond) and less-dissipative, more efficient electromechanical coupling (e.g., room-temperature magnetomotive, integrated piezoelectric schemes for parametric pumping) that could successfully scale up to VHF and UHF bands.

Acknowledgment. We thank S. Stryker for help with the experimental apparatus. We thank M. C. Cross, R. Lifshitz, and I. Kozinsky for helpful discussions. We are grateful to C. A. Zorman and M. Mehregany for providing SiC material used in making the devices. We are grateful to J. Arlett for useful comments and discussions. We acknowledge financial support from DARPA/SPAWAR under Grant N66001-02-1-8914.

References

(1) Nayfeh, A. H.; Mook, D. T. *Nonlinear Oscillations*; Wiley: New York, 1979.
(2) Wu, L.; Kimble, H. J.; Hall, J. L.; Wu, H. *Phys. Rev. Lett.* **1986**, *57*, 20.
(3) Movshovich, R.; Yurke, B.; Kaminsky, P. G.; Smith, A. D.; Silver, A. H.; Simon, R. W. *Phys. Rev. Lett.* **1990**, *65*, 1419.
(4) Esarey, E.; Sprangle, P.; Krall, J.; Ting, A. *IEEE Trans. Plasma Sci.* **1996**, *24*, 252.
(5) Hines, M. E. *IEEE Trans. Microwave Theory Tech.* **1986**, MTT-32, 1097.
(6) Rugar, D.; Grütter, P. *Phys. Rev. Lett.* **1991**, *67*, 699.
(7) Turner, K. L.; Miller, S. A.; MacDonald, N. C.; Strogatz, S. H.; Adams, S. G. *Nature* **1998**, *396*, 149.
(8) Zhang, W. H.; Turner, K. L. *Sens. Actuators, A* **2005**, *122*, 23.
(9) Carr, D. W.; Evoy, S.; Sekaric, L.; Craighead, H. G.; Parpia, J. M. *Appl. Phys. Lett.* **2000**, *77*, 1545.
(10) Lifshitz, R.; Cross, M. C. *Phys. Rev. B* **2003**, *67*, 134302.
(11) Dana, A.; Ho, F.; Yamamoto, Y. *Appl. Phys. Lett.* **1998**, *72*, 1152.
(12) Moreno-Moreno, M.; Raman, A.; Gomez-Herrero, J.; Reifenberger, R. *Appl. Phys. Lett.* **2006**, *88*, 193108.
(13) Roukes, M. L. *Phys. World* **2001**, *14*, 25.
(14) Huang, X. M. H.; Zorman, C. A.; Mehregany, M.; Roukes, M. L. *Nature* **2003**, *421*, 496.
(15) Ekinci, K. L.; Roukes, M. L. *Rev. Sci. Instrum.* **2005**, *76*, 061101.
(16) Yang, Y. T.; Callegari, C.; Feng, X. L.; Ekinci, K. L.; Roukes, M. L. *Nano Lett.* **2006**, *6*, 583.
(17) Feng, X. L.; White, C. J.; Hajimiri, A.; Roukes, M. L. *Nat. Nanotechnol.* **2008**, *3*, 342.
(18) LaHaye, M. D.; Buu, O.; Camarota, B.; Schwab, K. C. *Science* **2004**, *304*, 74.
(19) Greywall, D. S.; Yurke, B.; Busch, P. A.; Pargellis, A. N.; Willett, R. L. *Phys. Rev. Lett.* **1994**, *72*, 2992.
(20) Postma, H. W. C.; Kozinsky, I.; Husain, A.; Roukes, M. L. *Appl. Phys. Lett.* **2005**, *86*, 223105.
(21) Harrington, D. A. Ph.D. Thesis, California Institute of Technology, 2002.
(22) Yu, M. F.; Wagner, G. J.; Ruoff, R. S.; Dyer, M. J. *Phys. Rev. B* **2002**, *66*, 073406.
(23) Feng, X. L.; He, R. R.; Yang, P. D.; Roukes, M. L. *Nano Lett.* **2007**, *7*, 1953.
(24) The finite element simulations have been done using CFDRC package by ESI Software.
(25) Cleland, A. N.; Roukes, M. L. *Sens. Actuators, A* **1999**, *72*, 256.
(26) Schoelkopf, R. J.; Wahlgren, P.; Kozhevnikov, A. A.; Delsing, P.; Prober, D. E. *Science* **1998**, *280*, 1238.
(27) Timoshenko, S.; Young, D. H.; Weaver, W., Jr. *Vibration Problems in Engineering*; Wiley: New York, 1974.
(28) Lifshitz, R.; Cross, M. C. *Rev. Nonlinear Dyn. Complexity* **2008**, *1*, 1.
(29) Feng, X. L.; Zorman, C. A.; Mehregany, M.; Roukes, M. L. *Tech. Digest, Solid-State Sensors, Actuators and Microsystems Workshop*, Hilton Head, South Carolina, June 4−8, **2006**, 86.
(30) Ekinci, K. L.; Yang, Y. T.; Roukes, M. L. *J. Appl. Phys.* **2004**, *95*, 2682.
(31) Gantmakher, V. F. *Rep. Prog. Phys.* **1974**, *37*, 317.
(32) Swartz, E. T.; Pohl, R. O. *Rev. Mod. Phys.* **1989**, *61*, 31.
(33) Kading, O. W.; Shurk, H.; Goodson, K. E. *Appl. Phys. Lett.* **1994**, *65*, 13.
(34) Ashcroft, N. W.; Mermin, N. D. *Solid State Physics*; Sanders College Publishing: New York, 1976.
(35) Fon, W. C.; Schwab, K. C.; Worlock, J. M.; Roukes, M. L. *Phys. Rev. B* **2002**, *66*, 045302.
(36) Mohanty, P.; Harrington, D. A.; Ekinci, K. L.; Yang, Y. T.; Murphy, M. J.; Roukes, M. L. *Phys. Rev. B* **2002**, *66*, 085416.
(37) Li, D. Y.; Wu, Y. Y.; Kim, P.; Shi, L.; Yang, P. D.; Majumdar, A. *Appl. Phys. Lett.* **2003**, *83*, 2934.
(38) Cleland, A. N. *New J. Phys.* **2005**, *7*, 235.

NL901057C